RESEARCH ARTICLE

Editor's Choice

ADVANCED
ENGINEERING
MATERIALS

www.aem-journal.com

On the Reliability of Automated Analysis of Fracture Surfaces Using a Novel Computer Vision-Based Tool

Anna Engelhardt,* Jens Decke, David Meier, Franz Dulig, Rishan Ragunathan, Thomas Wegener, Bernhard Sick, and Thomas Niendorf

Fracture surface analysis is of utmost importance with respect to structural integrity of metallic materials. This especially holds true for additively manufactured materials. Despite an increasing trend of automatization of testing methods, the analysis and classification of fatigue fracture surface images is commonly done manually by experts. Although this leads to correct results in most cases, it has several disadvantages, e.g., the need of a huge knowledge base to interpret images correctly. In present work, an unsupervised tool for analysis of overview images of fatigue fracture surface images is developed to support nonexperienced users to identify the origin of the fracture. The tool is developed using fracture surface images of additively manufactured Ti6Al4V specimens fatigued in the high-cycle-fatigue regime and is based on the identification of river marks. Several recording parameters seem to have no significant influence on the results as long as preprocessing settings are adapted. Moreover, it is possible to analyze images of other materials with the tool as long as the fracture surfaces contain river marks. However, special features like multiple origins or origins located in direct vicinity to the surface, e.g., caused by increased plastic strains, require a further tool development or alternative approaches.

A. Engelhardt, T. Wegener, T. Niendorf
Institute of Materials Engineering
Metallic Materials
University of Kassel
Kassel 34125, Germany
E-mail: a.engelhardt@uni-kassel.de

J. Decke, D. Meier, F. Dulig, R. Ragunathan, B. Sick
Intelligent Embedded Systems
University of Kassel
Kassel 34121, Germany

D. Meier
Helmholtz-Zentrum Berlin für Materialien und Energie
Berlin 14109, Germany

D. Meier
Artificial Intelligence Methods for Experiment Design (AIM-ED)
Joint Lab Helmholtz-Zentrum Berlin für Materialien und Energie (HZB)
and University of Kassel
Berlin 14109, Germany

The ORCID identification number(s) for the author(s) of this article can be found under https://doi.org/10.1002/adem.202300876.

1. Introduction

Microscopy images and their analysis play a decisive role in many investigations in materials engineering. Despite the high frequency of this task, analysis and classification of microscopy images are commonly done manually by experts, which in most cases leads to correct results.[1,2] However, a manual analysis is very time-consuming, causes high costs, and the effort multiplies with an increasing number of specimens or images. In addition, the results of the analysis strongly depend on the knowledge of the involved expert, so that the results can vary and will always be subjective.[1,3,4] A huge knowledge base is necessary to interpret images correctly, leading to misinterpretations, huge sticking points for beginners, and an enormous loss of knowledge in case of personnel turnovers. Moreover, manual analysis of microscopy images is often limited to a qualitative analysis, and quantitative statements cannot be made.[2,3] Due to these issues, many attempts were made to develop and use methods of automatic analysis of microscopy images leading not only to time and cost-reduction but also to objective,[4] reliable, and reproducible[3] results and quantitative determination[3] of microstructural features. However, the development of automatical analysis methods is difficult since the image appearance can vary in a wide range due to numerous factors influencing microscopy images including the considered material (e.g., history and preparation), the used microscope and camera, the chosen settings (e.g., magnification, light intensity, exposure time, file format), the surroundings (e.g., lighting conditions), and the user (e.g., level of expertise). However, approaches for different tasks were developed successfully and even some image analysis systems commercially available in combination with microscopes exist.[5–7] Different studies show that such commercially available software can be used, e.g., to determine morphological parameters of irregular graphite particles in cast iron[3] or of the second phase of dual-phase steels with a ferritic matrix.[4] However, details in the workflow of commercially available software often remain unclear and commercial software limits the opportunities to features and functionality provided by the software, which may not fully meet the needs of the customer's application. Moreover, the time needed to learn special software, licensing costs, and the limited level of customization

and access to the source code create the need to develop, maintain, and improve own approaches and codes.

Therefore, approaches were developed considering different materials, microscope types (light optical microscope [LOM] or scanning electron microscope [SEM]) and tasks. In the study of Liu et al.,[8] SEM images of AlSi10Mg processed by laser powder bed fusion (PBF-LB/M) were converted into binary images to analyze morphology features of the eutectic, cellular Al–Si microstructure. Morales-Rivas et al.[9] used an automated image processing procedure based on the Canny method to detect grain boundaries on polarized LOM images of an α-Ti-based alloy. Another approach[4,10] used a combination of LOM and SEM images to segment and analyze the second phase of dual-phase steels.

In the past years, an increasing number of studies deal with the use of deep learning (DL) methods to analyze microscopy images. In the study of Masci et al.,[11] a max-pooling convolutional neural network (CNN) was used to classify defects in rolled steel strip with the aim to use the method in a real production line as a fast and reliable automated machine vision inspection. Based on the approach mentioned above,[4,10] Azimi et al.[1] developed a fully CNN accompanied by a max-voting scheme to classify the second phase of a low-carbon steel with a ferritic matrix based on SEM images. Although, DL methods could lead to very promising results, their disadvantage is the big amount of data being needed.[12] Although it is possible to create an applicable database in some cases, e.g., using extracted phases as input objects,[1] in many cases the database is restricted and leads to results being characterized by low reliability. Moreover, supervised DL (an approach where an algorithm is trained to make predictions or decisions based on input data that is labeled with the correct output or target value) suffers from the limitation that it requires a set of labeled input–output pairs to train the model. The annotation and labeling of data is a particularly time-consuming and complex process that must be manually carried out by experts eventually entailing the risk of inclusion of numerous uncertainties.[12,13]

The aforementioned studies show that different tasks can be implemented as automatical analysis of microscopy images. However, all these studies consider images of micrographs and, with it, represent a part of the analysis of microscopy images only. The assessment of fracture surface images, also referred to as fractography, represents another important part in the field of microscopy image analysis. The fractography as part of fatigue testing, e.g., creates insights into the failure of specimens or components by analyzing topographic features of the fracture surface and links them to the different operating fracture mechanisms, external conditions, and causes of failure.[2,14,15] Closely related to the analysis of micrographs, the fractography has identical problems, e.g., easily done misinterpretation.[2] However, the automatization of fractography is much more complex due to the higher complexity of fractographic images including 3D of fractures[14] and the wide variation of characteristics belonging to the same kind of fracture mechanism.[15] This higher complexity hinders an automatical analysis, e.g., the segmentation of topographic features requires more effort.[14] Nevertheless, an automatical analysis of fracture surface images would lead to a faster and more accurate assessment.[15] Therefore, it has been a topic of research since decades. Yang et al.[16] developed an approach to quantify the percentage areas of intergranular

and transgranular fractures of ceramics and ceramic matrix composites using the gradient of SEM line scanning profiles. Furthermore, Komai et al.[17] used a soft clustering method to classify textural features of six different fracture surface morphologies on SEM images. Since then, only a few studies dealt with the assessment of fracture surface images, e.g., an approach was developed for the segmentation of fracture surface images by multilevel thresholding.[14] Similar to the trends detailed for analysis of micrographs, the use of DL methods to automatically analyze fracture surface images has increased during the past years. Tsopanidis et al.[2] used a pretrained CNN with a U-net architecture to characterize transgranular and intergranular fractures on SEM images of a ceramic material system and reached high prediction accuracy. In another study,[15] four different fracture surface types of metallic materials (ductile, brittle, fatigue, and corrosion fatigue) were classified among others with different pretrained CNN using real-scale fracture images and SEM images with different scales as training data. Instead of classifying different types of surface fractures, the study of Wang et al.[12] tried to detect the fatigue crack initiation sites on fracture surface images using a deeply supervised object detector. Due to a limited training dataset, the results were reasonable but not accurate enough for a practical application.

As pointed out, different approaches to automatically analyze fracture surface images were developed in the past. However, a reliable tool considering different aspects of fracture surface images is still missing. In all aforementioned studies dealing with fractography, detail images were used. Although this approach enables the enhancement of the used data by dividing one image into different smaller images, it is unfavorable because it presumes that the user has enough experience to capture images of interesting areas. Therefore, in the present study, an unsupervised tool to analyze overview images of fracture surfaces was developed supporting nonexperienced users to orientate on the fracture surface, find important features, and capture images of them. Eventually, the tool developed within the present study will help any nonexpert to prevent misinterpretations and overcome roadblocks. Moreover, the underlying algorithm could be used for a fully automated analysis of a large number of fracture surface images reducing time and costs and finally enable objective and reproducible results. With a further development of the algorithm in the future, quantitative statements could be made and expert knowledge could be integrated so that a loss of knowledge in case of personnel turnovers is avoided. Eventually, already existing analysis tools using detailed images could be integrated in the tool in the future. Due to the complexity of the tool in focus, the development was divided into different steps. As a first step, a tool locating the origin of the fracture, i.e., the crack initiation site, on fracture surface images was developed. Considering the results of Wang et al.,[12] computer vision techniques instead of DL methods were used. As base for the development, images of additively manufactured Ti6Al4V specimens fatigued in the high-cycle-fatigue (HCF) regime were used. Based on these images, features that could be used in an automated assessment were identified. Based on these features, a tool was developed to locate the origin of the fracture on the images. Afterward, the reliability of the developed tool was analyzed by evaluation of the influence of different recording parameters. As last step, the tool was tested with images with more complex

features and images of other materials to investigate the opportunities and limitations of the developed tool.

2. Experimental Section

2.1. Considered Material

As base for the tool development, specimens of additively manufactured Ti6Al4V were used. All considered specimens were produced in electron beam-based powder bed fusion (PBF-EB/M) with an ARCAM A2X PBF-EB/M system from Arcam AB (Mölndal, Sweden) as rectangular cuboids ($40 \times 40 \times 10$ mm³). From these cuboids, flat dog-bone shaped fatigue specimens with nominal gauge cross sections of 3 mm × 1.6 mm (e.g., used in ref. [18]) were cut by electrodischarge machining (EDM), mechanically ground down to 12 μm grit size, and examined in stress-controlled HCF tests. The loading direction was parallel to the build direction (BD) during the fatigue tests. Overall, 11 pairs of fracture surfaces, i.e., 22 fracture surfaces, were considered, respectively. The corresponding fatigue data were not analyzed in the present study.

The specimens were used to collect overview images of the fracture surfaces with a SEM CamScan MV2300 operating at 20 kV. A probe current PC of 8 and a scan speed ν of 4 was used to capture the images. During image capturing, most recording parameters were kept constant, but some recording parameters had to be adapted to every specimen individually. However, it was tried to keep those parameters in a similar range. One important parameter that had to be varied was the working distance WD as the fracture surfaces were not cut from the specimens so that every fracture surface had an individual height. The magnification Mag was chosen so that the area of the fracture surface was maximized in the captured image, leading to magnifications between 80× and 95×. Moreover, the parameters of brightness and contrast, i.e., Gain and Black had to be varied for each specimen to capture the individual features of the fracture specimens clearly.

To investigate the influence of the different recording parameters on the results elaborated by the tool developed, a second set of images of one selected specimen of Ti6Al4V (HCF) were taken with varied recording parameters. In addition, this simulates image capturing by different users. Based on a reference set of recording parameters, which is shown in **Table 1**, the working distance WD, the magnification Mag, the scan speed ν, the probe current PC, and the parameters of brightness and contrast (Gain

and Black) were varied. Due to the high amount of required time, the task was divided into two parts. In the first part, WD, Mag, and ν were varied based on reference parameter set 1 (R1). In the second part, PC, Gain, and Black were varied based on reference parameter set 2 (R2). The reference Gain and Black of the second part differs from the parameters in the first part, since the SEM filament had to be changed meanwhile. However, the parameters resulted in similar image appearances. An adjustment of Gain was necessary for the investigation of the influence of the PC. Without this adjustment, the images became brighter with decreasing PC so that no details were visible on the image at PC = 4.

As last step, the tool was applied to images with special features (multiple failure origins), images of specimens fatigued in the low-cycle-fatigue (LCF) regime being characterized by higher plastic strains as compared to the HCF regime as well as images of another additively manufactured material fatigued in the HCF regime (AlSi12). These images were captured with the already-mentioned SEM using different recording parameters, which were adapted to the particular specimen. All considered AlSi12 specimens were cut by EDM from rectangular cuboids ($20 \times 8 \times 50$ mm³) manufactured by PBF-LB/M using a SLM 280^{HL} system from SLM Solutions Group AG (Lübeck, Germany). For more details, the reader is referred to another study.[18]

Figure 1 shows one of the used SEM images. Here, the image can be always divided into three areas. An area with information concerning the captured image is located at the bottom of the image. The captured image is above this area and can be divided into a background and the fracture surface. The fracture surfaces of all considered specimens had similar features. These features generally are well known in literature, e.g., detailed in[19] and therefore only explained briefly in the following. The three main features on fracture surfaces of fatigued specimens are the origin of the fracture, the fatigue fracture zone, and the overload failure zone.[12,19] The origin of the fracture is the point where the crack started.[19] In this study, the main focus was on the detection of the origin of the fracture; for this reason, the developed tool should be able to reliably detect this feature. All fracture surfaces considered had a single origin, which was easy identifiable. This relieved the verification of the tool results. The origin of the fracture is surrounded by the fatigue fracture zone. In this zone, the crack growth is relatively slowly.[19] The fatigue fracture zone can show features such as progression marks and river marks,[19] both containing information about crack growth. While progression marks (not observed in case of the considered specimens) indicate how the crack has grown across the surface, river marks indicate the direction of crack growth.[19] A high number of river marks was found on the considered fracture surfaces of Ti6Al4V fatigued in the HCF regime. From a graphical point of view, river marks are lines pointing at the origin of the fracture and, with it, contain information concerning the origin position. Therefore, river marks were thought to be most suitable to detect origins automatically and, thus, were chosen to be the feature used in the tool. The fatigue fracture zone is surrounded by the overload failure zone, which is related to very fast crack growth.[19] This zone is characterized by a rough surface and, thus, provided no information that could be useful for detecting the origin of the fracture. The ratios of the fatigue fracture zone and the overload failure zone differ depending on the material and the fatigue

Table 1. Reference sets of recording parameters used for the investigation of the influence of the recording parameters on the results of the tool.

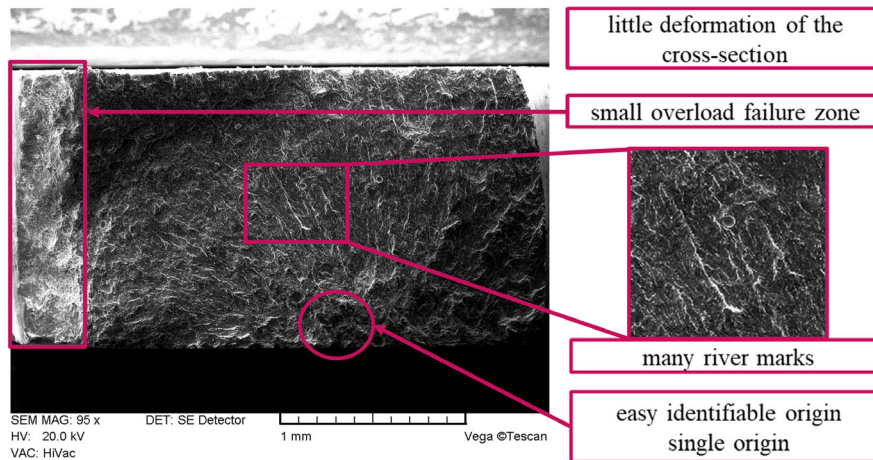|	R1	R2
WD in mm	26.1315	26.1315
Mag	90x	90x
PC	8	8
ν	4	4
Gain	37.8	37.0
Black	65.5	69.2

Figure 1. Example of the images used for the tool development with requirements that would be beneficial for an automatic analysis of surface fracture images. All images contain an area with information (located at the bottom of the image) and the actual image which can be divided into a background and the fracture surface.

regime, i.e., the degree of plastic deformation. On the considered fracture surfaces, the overload failure zone always was small, while the fatigue fracture zone was large. This increased the chance to achieve a high number of exploitable river marks and, thus, was expected to be beneficial for the tool. Since overview images were used, details such as fatigue striations, which only are visible under high magnification,[19] were not considered.

Another important feature for the automatical assessment is the shape of the cross section. In the present study, the shape of the considered specimens was limited to rectangular cross sections simplifying the separation of the fracture surface and the background in the images in the automated analysis. During fatigue testing, the cross section was deformed. However, the characterized Ti6Al4V specimens were only deformed slightly preserving the rectangular shape (similar to the original cross section). Thus, preprocessing steps dealing with the separation of the fracture surface and the background were minimized further.

2.2. The Developed Tool

In this section, the developed tool for the origin detection is presented. For this purpose, the fundamental procedure is shown in **Figure 2**a, which will be explained in the following. In order to detect the origins in an automated manner, some preprocessing steps were necessary. The images were composed of the actual fracture surface, the background, and information about the recording (see Section 2.1). For the recognition tool, only the fracture surface was of interest. Therefore, the images were cropped at first. An accurate method found was to increase the contrast of the images to distinguish between the area of the fracture surface and the background. With the use of the Canny edge detection algorithm, the actual area of the fracture surface could be identified and cropped from the image.[20] The adjustments of the contrast were dynamically adapted and depended on the average pixel value of the original image.
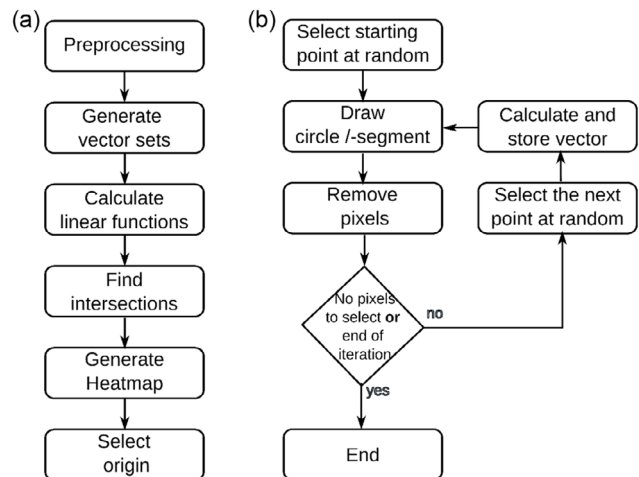

Figure 2. a) Flowchart of the proposed pipeline to determine automated fracture detection and b) detailed flowchart of the generation of vector sets.

The developed tool attempts to detect all river marks based on a cyclic search. Curve-like trajectories are also considered and approximated as accurately as possible at the end. A detailed overview on how the tool determines these trajectories can be seen in Figure 2b. At the beginning, the preprocessed image was divided into equally sized square images. Within each of these subimages, the pixel with the highest intensity value within the specific subimage was considered for further investigation. From these pixels, one was randomly selected and was used as the starting point for the subsequent search. A threshold value was calculated from the selected starting point. This procedure allowed to define a minimum pixel value to filter pixels to be considered for the further process. In this way, river marks that do not have the maximum pixel value of 255 still could be detected. For each starting point, a circle with a fixed radius was drawn. Within this circle all pixels were deleted, which were below the determined

threshold. From the resulting set of points, the next point was selected and used for further search. A direction was predefined taking into account the starting point and the identified second point. The vector that could be determined from these points was now used to draw a circle segment with defined angles on the second point. The central axis of this segment was oriented with respect to the previously determined vector. The basic concept assumed that this vector is a part of a river mark and, thus, only points in this direction were of further interest. Then again (within the next circle segment) all points below the threshold were deleted and from the remaining ones another point was selected. The already selected point was also excluded by setting its value to 0 for further search. This also limited that different starting points did not result in the same vectors. Next the resulting vector was determined and in the same way as before the circle segment was drawn in. Afterwards, the next point was selected. This process was repeated for each starting point until there were no more points within the next circle segment or a previously determined number of iterations was accomplished. The size of the radius plays an important role as a hyperparameter controlling the detection of river marks. It determines the size of river marks to be detected. If the radius is selected too large, the algorithm could miss fine river marks. Conversely, if the radius is too small, the output will be too noisy. The presented procedure is depicted in **Figure 3**a where a detailed view of a single search is shown, while Figure 3b presents a preprocessed fracture image and a completed search for all starting points.

During this process, a list was created for each starting point, in which the individual vectors were stored. After the search was completed, all vector sets with a too large angular variance were sorted out, because they most likely did not describe a river mark. From the remaining vector sets, a weighed vector was determined, which was to represent the chain of the vectors optimally. In order to consider possible curves, the weighed average value of these vectors was calculated. The vectors were weighed linearly at their recognition time. Thus, the last recognized directions had a more pronounced influence on the resulting line than the first recognized ones. From the vector calculated in this way, a linear function was determined. This line pointed in the direction of the averaged vector and ran through the last point of the previous search. After this process was completed for all vector sets, the result was a set of linear functions which ideally described the fracture trajectories (river marks). All intersections of these functions were calculated from these linear functions. In order to be able to determine where the origin of the fracture could be found, a heatmap was plotted. This heatmap was compiled as a 2D Gaussian distribution at each determined intersection point. The mean value of the Gaussian distribution corresponded to the coordinates of the intersection of two straight lines and the standard deviation was empirically set to the constant value of 0.3. These individual Gaussian curves were summed up, finally providing a heatmap that points at the area with the most intersections and, thus, the region of the origin of the fracture (ROF) on the fatigue fracture surface.

3. Results

The tool could correctly detect the ROF in case of most images analyzed. However, the accuracy of the results varied. During analysis, the starting points on the river marks are selected randomly and, therefore, change in every analysis. While this is useful for analysis of different images (since river marks vary on each image), it might cause problems with respect to repeatability. Therefore, it was important to investigate if the repeated assessment of one image leads to similar results. Three images captured with the scan speed of $v = \{0, 4, 8\}$ were analyzed multiple times for this assessment. The results are shown in **Figure 4**. Considering a constant v, the repeated analysis of an image leads to similar results. However, the quality of the results depends on the applied v. Using $v = 0$, the image is not cut correctly, i.e., in such a way that the resulting image contains parts of the background and the upper edge of the fracture surface. As a result the ROF cannot be detected. Nevertheless, a small but not high-rated area was detected in the ROF. Considering $v = 4$ and $v = 8$, the resulting image is cut correctly containing the fracture surface only. Moreover, the ROF is detected correctly. In most cases, $v = 4$ leads to the smallest detected areas.
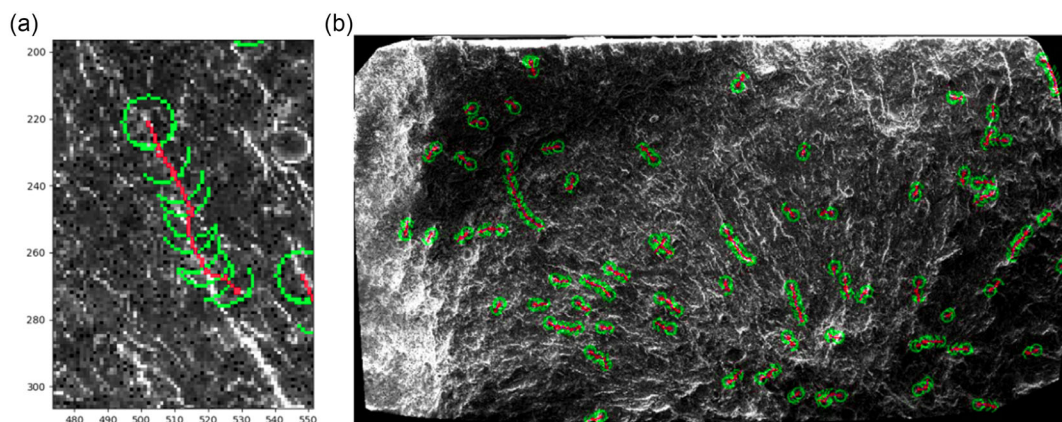

Figure 3. Results for vector search: a) single search and b) complete search. The single search (a) is a partial image of the complete search (b). The starting point of the search is indicated by the green circle. The red line is used to show the direction. Circle segments are used in each iteration step. The direction of subsequent search is possible only within these circle segments.
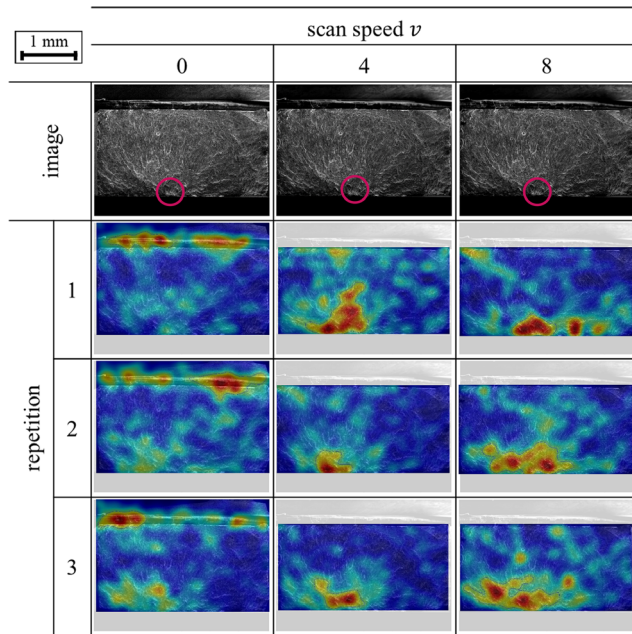
Figure 4. Results of the developed tool for repeated assessments. The three considered images were recorded with different v. The origin of the fracture is marked in the original image using a red circle. The results of each analysis are shown superimposed to the original image (light gray) to mark the position of the cut image and simplify the evaluation of the detected region of the origin of the fracture.

Figure 5. Results of the developed tool for images captured with different recording parameters (exemplary selection). The considered fracture surface is similar to the fracture surface shown in Figure 4. The results of each analysis are shown superimposed to the original image (light grey) to mark the position of the cut image and simplify the evaluation of the detected region of the origin. Dark regions, e.g., in the row "PC", are areas excluded in preprocessing.

As mentioned earlier, the influence of the recording parameters on the results determined by the tool was examined. Therefore, the working distance WD, the magnification Mag, the scan speed v, the probe current PC, and the parameters of brightness and contrast (Gain and Black) were changed systematically. The corresponding results are shown in **Figure 5** (with the exception of the results of v, which were already detailed in Figure 4).

Images captured with different WD were cut correctly and the ROF was also detected correctly. However, the results of WD = 20 mm show a second detected area in the upper-left corner of the resulting image. Considering images with increasing Mag values, the size of the cut region increases, as well. Nevertheless, the ROF is detected correctly in all images. However, the detected area is slightly shifted in case of Mag = 70×. In case of Mag = 90×, the detected area is larger than in the other cases. All images with different PC values are cut correctly. Considering PC = 2, the ROF is detected correctly, as well. In the resulting image of PC = 6, the ROF is detected as one of several marked areas, and in the resulting image of PC = 8 the detected area is slightly shifted with respect to the ROF. Considering the image with Gain = 39, the fracture surface is cut correctly and the ROF is detected correctly. With decreasing Gain, a smaller region is cut. With that, a too small region only containing parts of the origin is cut from the image with Gain = 35. Thus, a so that correct detection is not possible. The region cut of the image with Gain = 37 contains the ROF. More than one possible area was detected, however, with the correct one being among them. With different values of Black, again a region smaller than the fracture surface is cut. Nevertheless,
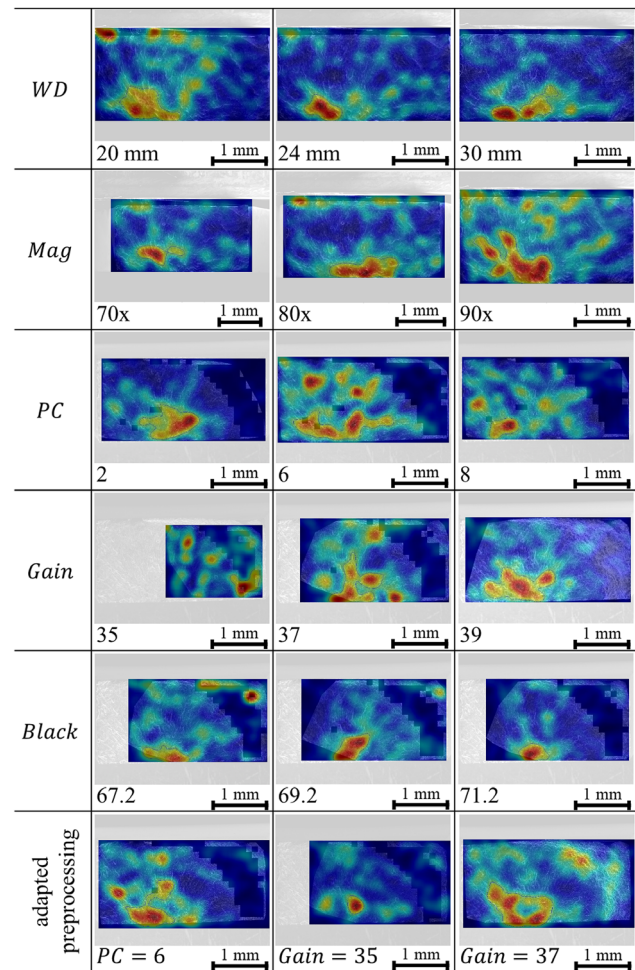
the ROF is detected correctly for all three considered values. The precision with respect to the detected areas was improved with adapted settings in preprocessing (exemplarily shown in Figure 5 using some images leading to wrong results before).

As the final step, the tool was used to analyze images with special features and images of other materials and fatigue regimes, respectively. A Ti6Al4V specimen fatigued in the HCF regime with multiple origins was used to assess the results of images with special features. The image is shown in **Figure 6** and the two origins located in the corners of the specimen are marked by red circles. The tool determined two areas for the origin: one in the middle of the specimen and one at the right corner where one of the ROFs is located.

An image of a Ti6Al4V specimen fatigued in the LCF regime was used to investigate the transferability of the tool to images related to other fatigue regimes. Corresponding images show many river marks and easily identifiable origins. However, the
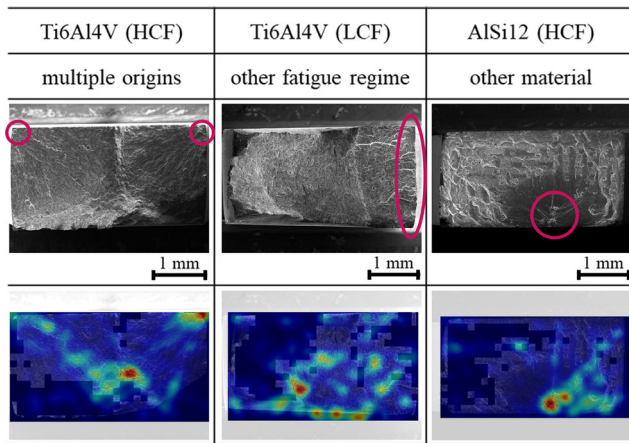
Ti6Al4V (HCF)	Ti6Al4V (LCF)	AlSi12 (HCF)
multiple origins	other fatigue regime	other material

Figure 6. Examplary sets of results of the developed tool for fracture surface images with special features (multiple origins) and fracture surface images of other materials or fatigue regimes. The origin of the fracture is marked in the original image using a red circle.

fatigue zones are smaller than in case of the zones of the HCF specimens. Besides, specimens of Ti6Al4V (LCF) often have relatively large origins located in direct vicinity of the surface, as shown in Figure 6. For the shown example, the tool determines different areas within the overload failure zone as possible ROFs.

As last step, the transferability to images of other materials was tested. Therefore, images of AlSi12 fatigued in the HCF regime were used. The fracture surfaces of these specimens differ significantly from the fracture surfaces used to develop the tool. Although they are characterized by easily identifiable origins, which vary clearly from the fatigue zone, the number of river marks is low. Moreover, the fatigue zone is small, so the number of occurring river marks is reduced and their size comparatively small. Nevertheless, the tool determines the ROF correctly. (Some results shown were already presented at DVM Workshop "Grundlagen und Beispiele zur Digitalisierung für die Materialforschung und -prüfung", online, 2020.)

4. Discussion

In this section, the results presented in the previous section will be discussed with respect to reliability, reproducibility, as well as transferability. Comparing the results of the repeated analysis, the tool developed leads to reasonable and similar results independent from the starting points. The tool detects and follows the river marks from the starting point to obtain the direction pointing at the ROF. Thus, the location of the starting point on the river mark is thought to have a minor influence on the results. Still, it becomes apparent that the results of the developed tool vary slightly. Especially images captured with $v = 0$ lead to inaccurate and varying results. With increasing v, the results become more accurate. Therefore, the scan speed v, which defines the speed of the electron beam scanning the specimen, has a significant influence on the result. To capture images with $v = 0$, a high scan speed is used so that the electronic noise level of the image increases and the image is less clear.[21] This hinders robust analysis with the tool as the number of bright pixels is increased due

to the noise. However, the still detected, but not so high-rated, areas in the images indicate that the tool might lead to the correct result, as long as the image is cut correctly. The noise decreases with increasing v values and at $v = 6$ and $v = 8$ the noise is minimized to a level ensuring that the captured images are almost noise free. The results of $v = 8$ are outstanding, however, the use of such a slow scan speed is too time-consuming. Since the differences of the results in $v = 6$ and $v = 8$ are small, capturing images with $v = 6$ represents a promising compromise between quality of the results and capturing time.

The assessment of different recording parameters revealed different influences on the tool's results. The working distance WD describes the distance between the pole piece of the objective lens and the plane of best focus.[21] A small WD, i.e., locating the specimen close to the lens, leads to high image resolution and decreases the depth of field at the same time.[21] Therefore, details are less clear. This allows to rationalize the second detected area in the image with WD = 20 mm. Since details are less clear, the tool has problems detecting the river marks and, as a result, wrong areas are detected. With a larger WD, the depth of field increases.[21] The beam diameter also increases, leading to a lower resolution.[21] Moreover, the signal strength decreases and therefore, the image can appear relatively noisy.[21] However, this seems to have almost no detrimental influence on the results. This is in good agreement with the results obtained with varying v, i.e., relatively good stability against noise.

The magnification Mag is the ratio of the length of the image to the corresponding length of the specimen.[21] Since overview images of fracture surfaces should be analyzed by the tool, Mag is limited to relatively low values in the present study. With increasing magnification, the scanned area on the specimen gets smaller[21] and more information concerning details is captured on the image. With this, a decreasing Mag value leads to a more extensive background area in the images. Nevertheless, the fracture surfaces were cut correctly, even at small Mag values for all considered magnifications. A decreasing Mag value results in less pronounced details, as well. This could be a reason for the slightly shifted detected area in the case of Mag = 70×. Since less information is available on the image, the detection gets less accurate. In case of Mag = 90×, the detected area is larger than in the other cases. It is thought that at this magnification too many details are visible, hindering robust analysis by the tool. The magnification in turn depends on the WD,[21] so the interaction of both recording parameters should be investigated in future work.

The probe current PC is the current that impinges on the specimen generating various signals[21] like the secondary electrons being used for creating the images considered in the present work. The PC has a significant influence on the resolution of the images since it directly influences the beam size that hits the specimen (spot size).[21] Thereby, a high PC leads to a small spot size increasing the image resolution.[21] With that, details are pictured very clearly. Although this would be theoretically beneficial for the tool, the results at high PC values, e.g., PC = 8, are not accurate. Maybe the high number of details generates additional white lines hindering robust analysis by the tool, similar to the high magnification. Moreover, a small spot size results in higher scan times so it is more time-consuming. Using PC = 6, more than one area is detected with

**ADVANCED
SCIENCE NEWS**

www.advancedsciencenews.com

**ADVANCED
ENGINEERING
MATERIALS**

www.aem-journal.com

the correct one among them. Probably, this is an effect of the Gain, which must be adjusted to obtain a similar image appearance. Gain greatly influences the results determined by the tool as discussed later in the text. Therefore, the values of preprocessing must be adapted in the analysis. With an adaption of the values (see Figure 5), better results could be obtained, clarifying the importance of an adapted preprocessing. A low PC increases the spot size and can lead to grainy images, which could hide surface details.[21] Nevertheless, the ROF of the image with PC = 2 is detected correctly. Similar to the results obtained with varying v, this confirms the stability of the tool against noise. The influence of PC is closely related to the influence of v, which was discussed at the beginning of this section. The interaction of both parameters will be investigated in future work.

The brightness Gain and the contrast Black are two common parameters in image processing. With increasing Gain the number of brighter pixels increases, rendering the whole image brighter. Considering the results shown in Figure 5, the influence of Gain is high in the considered value range. Especially low and high Gain values (meaning very dark or bright images) lead to wrong results. Since the image gets darker with decreasing Gain, a bigger area is excluded by preprocessing, leading to a relatively small resulting image. With a decreasing area of the resulting image, the number of river marks and, with it, information that can be used in the tool decrease as well, so that a correct detection is hindered (see Gain = 37 in Figure 5). Eventually, the ROF is excluded from the resulting image, so that a correct detection is not possible (see Gain = 35 in Figure 5). Black, often referred to as contrast, controls the sharpness of the image. A high value leads to a sharper image, while a low value makes the image smoother. The influence of Black in the considered value range seems to be small. All wrong results detailed in this section are based on constant preprocessing settings. In case the settings of the preprocessing are adjusted for these images, none of the recording parameters at the end will have such a detrimental influence on the results of the tool and, eventually, good results can be achieved for all considered recording parameters (see Figure 5).

As last step of the tool assessment, images with special features and images of other materials and fatigue regimes were analyzed, respectively. Analysis of images with two origins leads to two detected areas, where one ROF is determined correctly. Instead of the second ROF, a region in the middle of the image was highlighted. The straight lines calculated by the river marks stemming from both origins intersect at this place. This leads to a maximum of intersection points and, eventually, to a wrong identified area. Nevertheless, the tool worked generally correct. The mistake is caused by the assumption that only one ROF or maximum of intersection points must be located in the image. To avoid this error in the future, additional filters could be used to classify essential properties of the image, enabling a division of the image and a single analysis of the subimages with the tool developed in present work. Alternatively, a tool could be developed that determines the number of origins in the image as the first step.

The ROF in the image of Ti6Al4V fatigued in the LCF regime (considering another fatigue regime) was determined wrong, although the settings in the preprocessing were adapted. Since the origin of the fracture is located in a large area in the direct vicinity of the surface, it is not characterized by one point where a maximum of the intersection points of straight lines exists. Instead, the straight lines point more or less parallel to the region of the origin. Here, another approach is necessary to detect the form of origins. Thus, the developed tool can not be used in this case.

The images of the other considered material (AlSi12 fatigued in HCF regime) are characterized by a small number of river marks. Although the small number of river marks was expected to cause problems in the ROF detection, the tool detects it correctly. This clearly indicates that the tool can be used with images of other materials as long as the fracture surfaces of these materials contain river marks. However, at this point it has to be noted that the settings of the preprocessing were adapted. Other approaches must be developed for materials not featuring any river marks. Besides, specimens featuring other cross sections, e.g., circular, or highly deformed cross sections could require other approaches or further improvements of the tool presented.

5. Summary and Conclusions

In the present study, a computer vision-based tool was developed and tested to automatically locate the origin of fracture on fatigue fracture surface images. The developed tool detects river marks on the fracture surface and calculates the ROF based on intersection points of directions being related to the detected river marks. The results of this approach vary slightly, but the detected ROF is always correct, providing an orientation for nonexperienced users. Moreover, recording parameters and, with it, different users seem to have no significant influence on the results as long as the preprocessing settings are adapted. To further improve the results, a two-stage approach based on the developed tool could be implemented, which analyzes an overview image of the specimen with the developed tool as a first step. Afterwards, a detailed image of the detected ROF could be captured and analyzed by the tool to locate the origin of the fracture exactly. To broaden the possible applications, a transfer of the developed tool to images of other materials is very important. First attempts show that such a transfer is possible in case the images contain river marks. Even good results with images containing only few river marks could be achieved with adjusted preprocessing settings. However, special features like multiple origins or origins located in relatively large areas in direct vicinity to the surface, being characteristic for other fatigue regimes, require a further development of the tool or alternative approaches.

Conflict of Interest

The authors declare no conflict of interest.

Author Contributions

A.E. took care of conceptualization, investigation, visualization, writing the original draft, and writing the review and editing. J.D. took care of investigation, visualization, writing the original draft, and writing the review and editing. D.M. took care of writing the review and editing. F.D. took care of methodology and software. R.R. took care of methodology and software. T.W. took care of writing the review and editing. B.S. took care of funding acquisition, project administration, resources, supervision, and writing the review and editing. T.N. took care of funding acquisition, project administration, resources, supervision, and writing the review and editing.

Data Availability Statement

The data that support the findings of this study are available from the corresponding author upon reasonable request.

Keywords

additive manufacturing, image recognition, object detection, scanning electron microscopes, Ti6Al4V

[1] S. M. Azimi, D. Britz, M. Engstler, M. Fritz, F. Mücklich, *Sci. Rep.* **2018**, *8*, 2128.
[2] S. Tsopanidis, R. H. Moreno, S. Osovski, *Eng. Fract. Mech.* **2020**, *231*, 106992.
[3] A. Velichko, F. Mücklich, *Prakt. Metallogr.* **2006**, *43*, 192.
[4] J. Gola, D. Britz, T. Staudt, M. Winter, A. S. Schneider, M. Ludovici, F. Mücklich, *Comput. Mater. Sci.* **2018**, *148*, 324.
[5] Carl Zeiss Microscopy Deutschland GmbH, https://www.micro-shop.zeiss.com/en/de/system/axiovision+software-software+axiovision-software/6014/ (accessed: March 2023).
[6] EVIDENT, https://www.olympus-ims.com/en/microscope/stream2/ (accessed: March 2023).
[7] KEYENCE Deutschland, https://www.keyence.co.uk/products/microscope/digital-microscope/vhx-7000/ (accessed: March 2023).
[8] Q. Liu, H. Wu, M. J. Paul, P. He, Z. Peng, B. Gludovatz, J. J. Kruzic, C. H. Wang, X. Li, *Acta Mater.* **2020**, *201*, 316.
[9] L. Morales-Rivas, S. Diederichs, L. Böhme, E. Gordo, A. Hebestreit, E. Kerscher, *Prakt. Metallogr.* **2018**, *55*, 678.
[10] D. Britz, J. Webel, J. Gola, F. Mücklich, *Prakt. Metallogr.* **2017**, *54*, 685.
[11] J. Masci, U. Meier, D. Ciresan, J. Schmidhuber, G. Fricout, *Proc. of the Inte. Joint Conf. on Neural Networks* June **2012**, pp. 1–6, http://dx.doi.org/10.1109/IJCNN.2012.6252468.
[12] S. Y. Wang, P. Z. Zhang, S. Y. Zhou, D. B. Wei, F. Ding, F. K. Li, *Comput. Mater. Sci.* **2020**, *171*, 109259.
[13] Y. Roh, G. Heo, S. E. Whang, *IEEE Trans. Knowl. Data Eng.* **2021**, *33*, 1328.
[14] R. Y. Kosarevych, O. Z. Student, L. M. Svirs'ka, B. P. Rusyn, H. M. Nykyforchyn, *Mater Sci* **2013**, *48*, 474.
[15] M. X. Bastidas-Rodriguez, L. Polania, A. Gruson, F. Prieto-Ortiz, *Eng. Fail. Anal.* **2020**, *113*, 104532.
[16] W.-J. Yang, C.-T. Yu, A. S. Kobayashi, *J Am. Ceram. Soc.* **1991**, *74*, 290.
[17] K. Komai, K. Minoshima, S. Ishii, *Trans. Jpn. Soc. Mech. Eng. A* **1991**, *57*, 2595.
[18] J. Richter, S. V. Sajadifar, T. Niendorf, *Addit. Manuf.* **2021**, *47*, 102346.
[19] N. W. Sachs, *J. Fail. Anal. Prev.* **2005**, *5*, 11.
[20] W. Rong, Z. Li, W. Zhang, L. Sun, *2014 IEEE Inter. Conf. on Mechatronics and Automation*, IEEE, Tianjin, China **2014**, p. 577.
[21] A. Ul-Hamid, in *A Beginners' Guide to Scanning Electron Microscopy*, Springer International Publishing, Cham **2018**.